

Impact of subsurface convective flows on the formation of sunspot magnetic field and energy build-up

Takafumi Kaneko,^{1,2*} Hideyuki Hotta,³ Shin Toriumi⁴ and Kanya Kusano⁵

¹Lockheed Martin Solar and Astrophysics Laboratory, 3251 Hanover Street B/252, Palo Alto, CA 94304, USA

²High Altitude Observatory, National Center for Atmospheric Research, P.O. Box 3000, Boulder, CO 80307, USA

³Department of Physics, Graduate School of Science, Chiba University, 1-33 Yayoi-cho, Inage-ku, Chiba 263-8522, Japan

⁴Institute of Space and Astronautical Science (ISAS)/Japan Aerospace Exploration Agency (JAXA), 3-1-1 Yoshinodai, Chuo-ku, Sagami-hara, Kanagawa 252-5210, Japan

⁵Institute for Space-Earth Environmental Research, Nagoya University, Furo-cho, Chikusa-ku, Nagoya, Aichi, 464-8601, Japan

Accepted XXX. Received YYY; in original form ZZZ

ABSTRACT

Strong solar flares occur in δ -spots characterized by the opposite-polarity magnetic fluxes in a single penumbra. Sunspot formation via flux emergence from the convection zone to the photosphere can be strongly affected by convective turbulent flows. It has not yet been shown how crucial convective flows are for the formation of δ -spots. The aim of this study is to reveal the impact of convective flows in the convection zone on the formation and evolution of sunspot magnetic fields. We simulated the emergence and transport of magnetic flux tubes in the convection zone using radiative magnetohydrodynamics code R2D2. We carried out 93 simulations by allocating the twisted flux tubes to different positions in the convection zone. As a result, both δ -type and β -type magnetic distributions were reproduced only by the differences in the convective flows surrounding the flux tubes. The δ -spots were formed by the collision of positive and negative magnetic fluxes on the photosphere. The unipolar and bipolar rotations of the δ -spots were driven by magnetic twist and writhe, transporting magnetic helicity from the convection zone to the corona. We detected a strong correlation between the distribution of the nonpotential magnetic field in the photosphere and the position of the downflow plume in the convection zone. The correlation could be detected 20–30 h before the flux emergence. The results suggest that high free energy regions in the photosphere can be predicted even before the magnetic flux appears in the photosphere by detecting the downflow profile in the convection zone.

Key words: MHD – sunspots – Sun: interior – Sun: photosphere – Sun: magnetic fields – Sun: flares

1 INTRODUCTION

δ -spots, characterized by opposite magnetic polarities in the same penumbra, frequently produce energetic events such as solar flares and coronal mass ejections. The relationship between the δ -spots and large flares have been studied for decades via observations of magnetic distribution and evolution (Zirin & Liggett 1987; Sammis et al. 2000; Toriumi et al. 2017; Kusano et al. 2020). δ -spots store a large amount of magnetic free energy that enables intense energy release as solar flares and eruptions. Revealing the mechanism of energy build-up in the complex magnetic distribution of the δ -spots is key to understanding and predicting the solar activity. Previous observations have detected the magnetic energy build-up by the emergence of new magnetic fluxes from the convection zones (Leka et al. 1996; Wheatland 2000; Georgoulis et al. 2012) and by the converging and shearing motions between the opposite-polarity magnetic fluxes in the photosphere (Schmieder et al. 1994; Park et al. 2018). Magnetohydrodynamic (MHD) simulations of the solar corona also demonstrated that flux emergence and photospheric motions can build up magnetic free energy and trigger flares and eruptions (Amari et al. 2000; DeVore & Antiochos 2000; Fan & Gibson 2007;

Kusano et al. 2012; Amari et al. 2014; Kaneko & Yokoyama 2014; Jiang et al. 2016; Kaneko et al. 2021).

The formation and evolution of δ -spots have been studied using both observational and theoretical approaches (Toriumi & Wang 2019). The properties of δ -spots have been revealed via direct measurements of the photospheric magnetic field. However, magnetic field evolution in the convection zone connected to the photosphere should be further studied because it cannot be measured directly. MHD simulations are effective methods to connect the evolution of magnetic field in the convection zone to photospheric magnetic evolution. A typical model is the twisted flux tube ascended by buoyant instability. To date, many MHD simulations with different parameters, e.g., twist number, buoyancy, number of flux tubes, and background magnetic fields, have been performed (Fan 2001; Magara & Longcope 2003; Fan 2009; Fang & Fan 2015; Takasao et al. 2015; Toriumi & Takasao 2017; Manek & Brummell 2021). These studies have revealed that highly kinked flux tubes with two sections of buoyant instability can reproduce the observed magnetic properties of δ -spots together with photospheric motions (Toriumi et al. 2014a; Fang & Fan 2015). In these simulations, the convectively unstable layer caused buoyant instability, whereas realistic convection with radiative heat transfer was not taken into account.

* E-mail: kaneko@lmsal.com

Background convection affects the transport of magnetic flux and sunspot formation. It is difficult to demonstrate the impact of convective flows deep in the convection zone on sunspot formation in the photosphere because self-consistent MHD simulations covering an area from the deep convection zone to the photosphere require large numerical resources due to the significant gaps in the typical time scale of the thermal convection and the speed of sound. Owing to the modern numerical techniques that reduce the gap of the characteristic speeds, sunspot formation in the photosphere can be directly reproduced with the effect of realistic convection in radiative MHD simulations (Cheung et al. 2010; Rempel & Cheung 2014; Chen et al. 2017; Toriumi & Hotta 2019; Hotta & Iijima 2020; Hotta & Toriumi 2020). Chen et al. (2017) demonstrated that flux emergence is driven by convective upflows, whereas the persistent strong magnetic field of the sunspots is formed in the subsurface downflow region. Although their initial flux tube model was reconstructed based on a self-consistent convective dynamo simulation (with temporal and spatial rescaling), the flux emergence simulation itself was carried out in a local box covering 30 Mm depth; thus, the impact of the convective flows in much deeper layers was not clear. The flux emergence simulations covering much deeper layer have been performed (Toriumi & Hotta 2019; Hotta et al. 2019; Hotta & Toriumi 2020). Toriumi & Hotta (2019) performed a flux emergence simulation with a deeper convection zone up to 140 Mm depth, which is very close to the bottom of the convection zone (200 Mm) given the large scale heights there. In their simulations, the flux tube was lifted upward at two sections by upflows and dragged downward by downflows in between them. The magnetic fluxes emerged by the upflows collided each other in the photosphere, leading to the formation of δ -spots. In addition, the rotational shearing motion was driven between the opposite-polarity fluxes due to the release of the magnetic twist, creating highly nonpotential fields (arcade field hosting a flux rope along the polarity inversion line). Hotta & Toriumi (2020) carried out a flux emergence simulation covering 200 Mm depth, reproducing the δ -spots with strong horizontal fields up to 6000 G, which was the maximum level in previous observations. They performed multiple simulations by changing the spatial resolution and the approximation method of radiation transfer (one-ray versus multi-rays). Comparison of the results showed that the amplification mechanism of the super-equipartition magnetic fields was the shearing motion between the rotating sunspots rooted to the deep convection zone.

In this study, we examined the impact of turbulent convective flows on the magnetic energy build-up associated with the formation of the δ -spots. We carried out a parameter survey by allocating the initial flux tube to different positions in the identical convection field. By analyzing the large number of simulated cases, we revealed the distribution trend of the nonpotential magnetic field in the photosphere and its relationship with the flow distribution in the convection zone. The remainder of the paper is structured as follows. Section 2 describes the setting of the numerical simulation. Section 3 shows the results of the calculations and statistical analysis. In Section 4, we summarize and discuss the results.

2 NUMERICAL SETTINGS

We solved the three-dimensional MHD equations including the radiative transfer equation.

$$\frac{\partial \rho_1}{\partial t} = -\frac{1}{\xi^2} \nabla \cdot (\rho \mathbf{v}), \quad (1)$$

$$\frac{\partial (\rho \mathbf{v})}{\partial t} = -\nabla \cdot (\rho \mathbf{v} \mathbf{v}) - \nabla p_1 + \rho_1 \mathbf{g} + \frac{1}{4\pi} (\nabla \times \mathbf{B}) \times \mathbf{B}, \quad (2)$$

$$\frac{\partial \mathbf{B}}{\partial t} = \nabla \times (\mathbf{v} \times \mathbf{B}), \quad (3)$$

$$\rho T \frac{\partial s_1}{\partial t} = \rho T (\mathbf{v} \cdot \nabla) s + Q, \quad (4)$$

$$p_1 = p_1(\rho, s), \quad (5)$$

$$\rho = \rho_0 + \rho_1, \quad (6)$$

$$p = p_0 + p_1, \quad (7)$$

$$s = s_0 + s_1, \quad (8)$$

where ρ , \mathbf{v} , \mathbf{B} , p , T , s , \mathbf{g} , Q , and ξ are the density, fluid velocity, magnetic field, gas pressure, temperature, entropy, gravitational acceleration in the vertical direction, radiative heating, and the factor of the reduced speed of sound technique (RSST), respectively. The subscript 0 denotes the variables of the stationary stratification in z -direction, and the subscript 1 denotes the perturbation. The background stratification was calculated using the hydrostatic equation based on Model S (Christensen-Dalsgaard et al. 1996). In Eq. (5), we used the equation of state considering the partial ionization effect with the OPAL repository (Rogers et al. 1996). See Hotta & Iijima (2020) for the details of the calculation procedure.

The calculations were carried out using the radiative MHD code R2D2¹ (Hotta et al. 2019). The MHD equations are solved using the four-step Runge Kutta method for time integration (Vögler et al. 2005) and fourth-order spatial derivative (Hotta & Iijima 2020) with the slope-limited artificial diffusion (Rempel 2014). The radiative transfer equation was solved by adopting the gray approximation and the Rosseland mean opacity. We only solved two rays for the radiative transfer equation: only upward and downward radiative energy transfers were considered. The horizontal radiative energy transfer should be included to reproduce the realistic solar convection by diffusing the horizontal small scale structures. In our simulations with a low spatial resolution, on the other hand, the realistic convection was eventually mimicked via the numerical diffusion. The high resolution simulations (e.g., Hotta & Toriumi 2020) should include the horizontal radiative energy transfer because the numerical diffusion is reduced. The RSST relaxed the Courant–Friedrichs–Lewy (CFL) condition dependent on the high sound speed in the photosphere (Hotta et al. 2012, 2015; Iijima et al. 2019). We set the RSST factor as follows:

$$\xi(z) = \max \left(1, \xi_0 \left[\frac{\rho_0(z)}{\rho_b} \right]^{1/3} \frac{c_s(z)}{c_b} \right), \quad (9)$$

where $\xi_0 = 160$ was adopted. $\rho_b = 0.2 \text{ g cm}^{-3}$ and $c_b = 2.2 \times 10^7 \text{ cm s}^{-1}$ were the density and sound speed around the base of the convection zone, respectively. $c_s = \sqrt{(\partial p / \partial \rho)_s}$ is the local adiabatic

¹ Radiation and RSST for Deep Dynamics

Table 1. Initial positions of the flux tubes

case	z_{tb}	y_{tb}
001–031	–22 Mm	3.072 Mm–95.232 Mm
032–062	–26 Mm	3.072 Mm–95.232 Mm
063–093	–30 Mm	3.072 Mm–95.232 Mm

speed of sound. We also limited the Alfvén speed up to 40 km/s to deal with the low- β region above the photosphere (Rempel et al. 2009).

The simulation domain is a rectangular box with the size of $0 < x < 98.3$ Mm, $0 < y < 98.3$ Mm, and -201 Mm $< z < 676$ km in Cartesian coordinates. The x – y plane represents the horizontal plane parallel to the solar surface, and the z -direction represents the height. $z = 0$ corresponds to $R = R_{\text{sun}}$, where R and R_{sun} represent the distance from the center of the Sun and the solar radius, respectively. To inhibit the convection cell larger than the solar supergranulation scale, we limit the horizontal size of the simulation domain within 100 Mm (see also Toriumi & Hotta (2019); Hotta et al. (2019)). The simulation domain covers the area from the deep convection zone to the lower chromosphere. In the vertical direction, uniform grid spacing was applied from the top boundary to $z = -4$ Mm with a grid size of $\Delta z = 48$ km. The grid size linearly increased from $z = -4$ Mm to the bottom boundary up to $\Delta z = 903$ km. Uniform grid spacing was applied in the horizontal direction with a grid size of $\Delta x = \Delta y = 128$ km. The total grid number was $768 \times 768 \times 512$. The periodic boundary condition was applied to the horizontal direction. The magnetic field in the bottom boundary was horizontal. The magnetic field in the top boundary was connected to the potential field.

First, we calculated the solar convection without a magnetic field until statistical equilibrium was achieved. We called this state as the initial state. Then, we introduced a magnetic flux tube into the convection zone. The magnetic field of the flux tube was calculated as a horizontal force-free field as follows:

$$B_x = B_{\text{tb}} J_0(\alpha r), \quad B_\phi = B_{\text{tb}} J_1(\alpha r), \quad (10)$$

where B_x and B_ϕ are the toroidal and poloidal components, respectively. r is the radial distance from the axis, $B_{\text{tb}} = 10^4$ G is the field strength of the axial magnetic field, J_0 and J_1 are the Bessel functions, $\alpha = a_0/R_{\text{tb}}$, $a_0 = 2.404825$, $R_{\text{tb}} = 8.5$ Mm. The flux tube had right-handed twist without writhe in the initial state. We carried out 93 simulations by allocating the initial flux tubes to 93 different positions. The initial positions of the flux tubes are summarized in Table 1. Figure 1 shows the initial positions of the flux tube axes against the background vertical velocity. The horizontal position y_{tb} was uniformly changed in the range of $24\Delta y$ – $744\Delta y$ (3.072 Mm–95.232 Mm) with an interval of $24\Delta y$ (3.072 Mm), corresponding to 31 different cases at the same depth. Note that the interval of 3 Mm was selected because the downflows had the small structures at this spatial scale as shown in Fig. 1. The depth z_{tb} was set to = –22 Mm (cases 001–031), –26 Mm (cases 032–062), and –30 Mm (cases 063–093). As shown in Fig. 1, the flow profiles at these depths were similar to each other. We show that the magnetic evolution from the different depths also resulted in a variety of the sunspot magnetic fields.

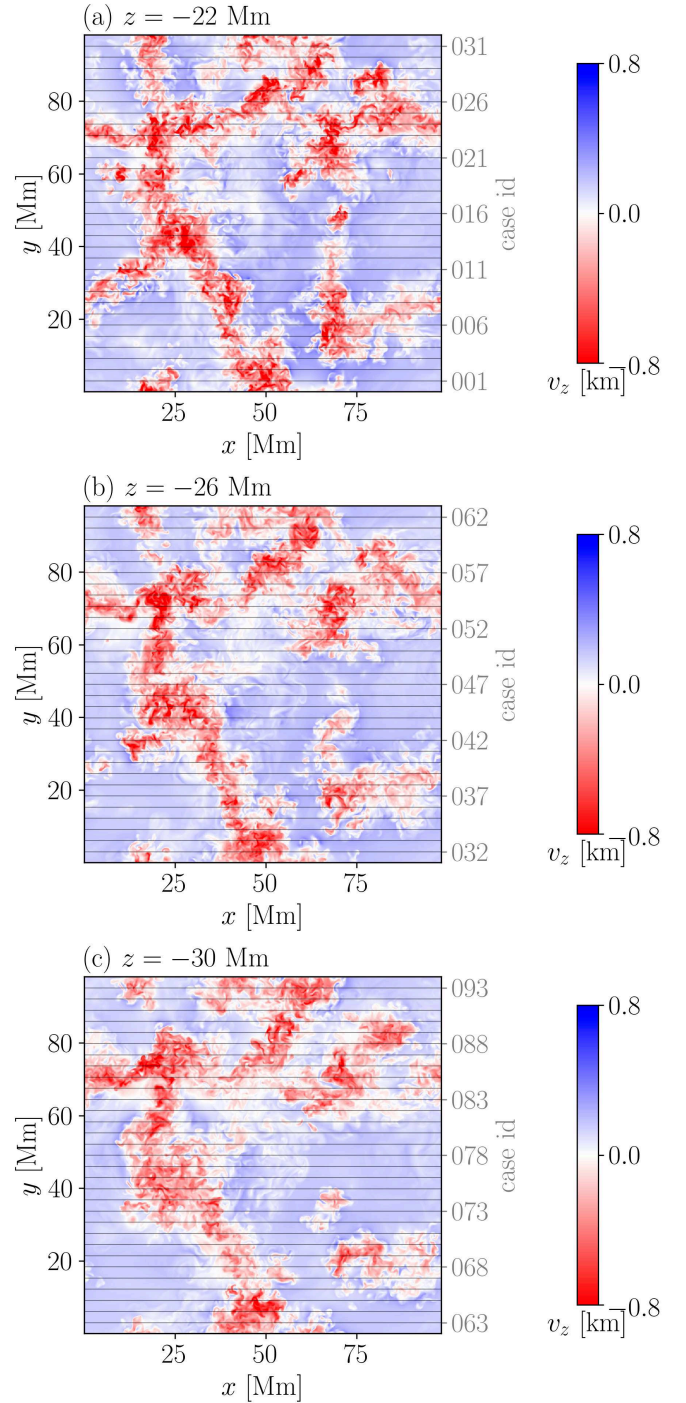


Figure 1. Initial positions of the flux tubes in the background vertical velocity. The gray lines represent the axial position of the flux tube in each case. The color represents vertical velocity v_z .

3 RESULTS

3.1 Typical case

Figure 2 represents the temporal evolution of the magnetic field in case 001 where δ -type magnetic distribution with a large spot area was reproduced. In this case, the opposite-polarity magnetic fluxes in the photosphere collided with each other, forming the δ -type magnetic distribution. Figure 3 represents the temporal evolution of the

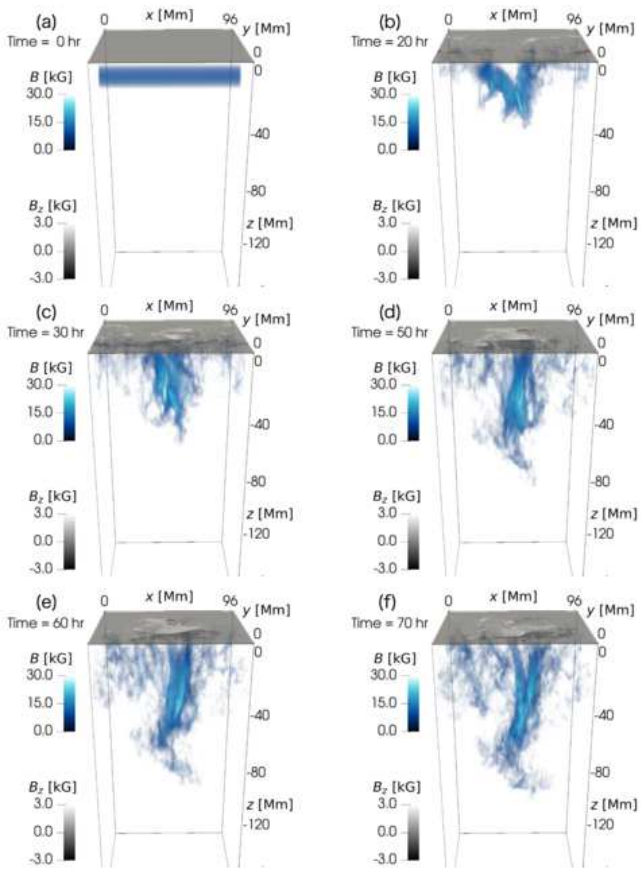


Figure 2. Temporal evolution of magnetic field in case 001. The grayscale represents the vertical magnetic field B_z at the $z = 0$ plane. Blue represents the field strength $|\mathbf{B}|$. Only the region where $|\mathbf{B}| > 3$ kG is rendered. For better visualization, the coordinate is horizontally translated as the initial flux tube position corresponds to the center in the y -direction.

vertical flows in case 001. The convective velocity field in our simulation included a persistent large-scale downflow plume extending to the deep layer. The downflow plume in the subsurface layer was also reproduced in the previous simulations (Stein & Nordlund 1989). Dragged by the downflow plume, the flux tube was deformed into the concave-up structure (Fig. 2(b)), and gradually sank to the deep convection zone. Meanwhile, the opposite-polarity magnetic fluxes in the photosphere approached each other and finally collided.

Figures 4 (a), (c), and (e) show the temporal evolution of the vertical magnetic field at the $\tau = 1$ surface. Figure 5 (a) and (b) show the time slice of B_z map along the circular slits with the different radii denoted by the yellow dashed circles in panels (a), (c), and (e). The center of the circular slits corresponds to the flux weighted centroid of the negative flux in each snapshot. Figure 5 (a) shows the clockwise rotational motion inside the negative flux (unipolar rotation) from the emergence time to $t = 55$ h. The clockwise rotation at the photosphere reduced the positive magnetic helicity of the flux tube in the convection zone, and increased the positive helicity over the photosphere, transporting the positive helicity from the convection zone to the corona. This motion is consistent with the previous numerical experiments without convection (Fan 2009; Sturrock et al. 2015) and with convection (Toriumi & Hotta 2019).

Figure 5 (b) represent the anti-clockwise rotation of the positive flux against the flux centroid of the negative flux (bipolar rotation). The driver of the anti-clockwise rotation was the conversion of the

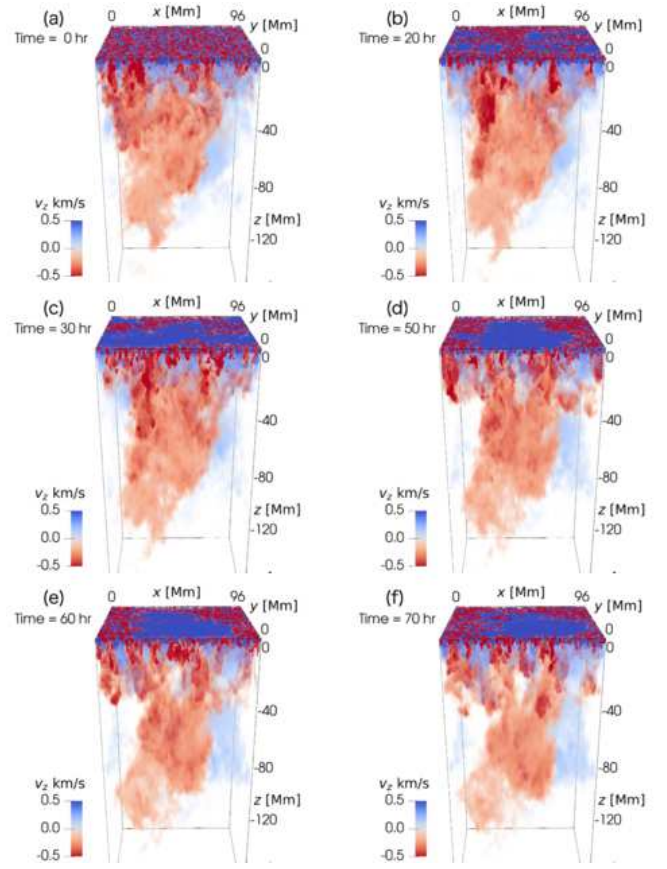


Figure 3. Temporal evolution of vertical flows v_z in case 001. Blue and red represent upflow and downflow, respectively. Only the regions where $|v_z| > 0.1$ km/s are rendered. The coordinate is the same as in Fig. 2.

twist to the writhe. Figure 6 shows the temporal evolution of the magnetic field lines in the convection zone during the anti-clockwise rotation. The positive writhe was created between the magnetic field lines connecting to the positive and negative fluxes at the photosphere. The helicity of the flux tube is described as the contributions from twist and writhe as follows,

$$\mathcal{H} = (\mathcal{T}_w + \mathcal{W}_r) \Phi^2, \quad (11)$$

where \mathcal{H} , \mathcal{T}_w , and \mathcal{W}_r represent helicity, twist, and writhe, respectively (Berger & Prior 2006). The initial straight flux tube had the positive helicity in the form of the right-handed twist. The right-handed twist is converted to the positive writhe as the positive and negative ends of the bending flux tube approached each other. The anti-clockwise motion between the positive and negative fluxes at the photosphere was driven by the increasing of the positive writhe.

As a proxy of flare productivity, we used nonpotential magnetic field defined as follows:

$$B_{np} = |\mathbf{B} - \mathbf{B}_{pot}|, \quad (12)$$

where \mathbf{B}_{pot} represents the potential field computed from the vertical component of magnetic field at the $\tau = 1$ surface. Note that, to mimic the analysis of the observational data, the height difference in the $\tau = 1$ surface (within 300 km) was not considered in the computation of \mathbf{B}_{pot} . Since the vertical components of \mathbf{B} and \mathbf{B}_{pot} are the same, B_{np} represents the difference in the horizontal components between \mathbf{B} and \mathbf{B}_{pot} . B_{np} is also associated with the magnetic free energy responsible for the maximum energy released by flares. Figures 4

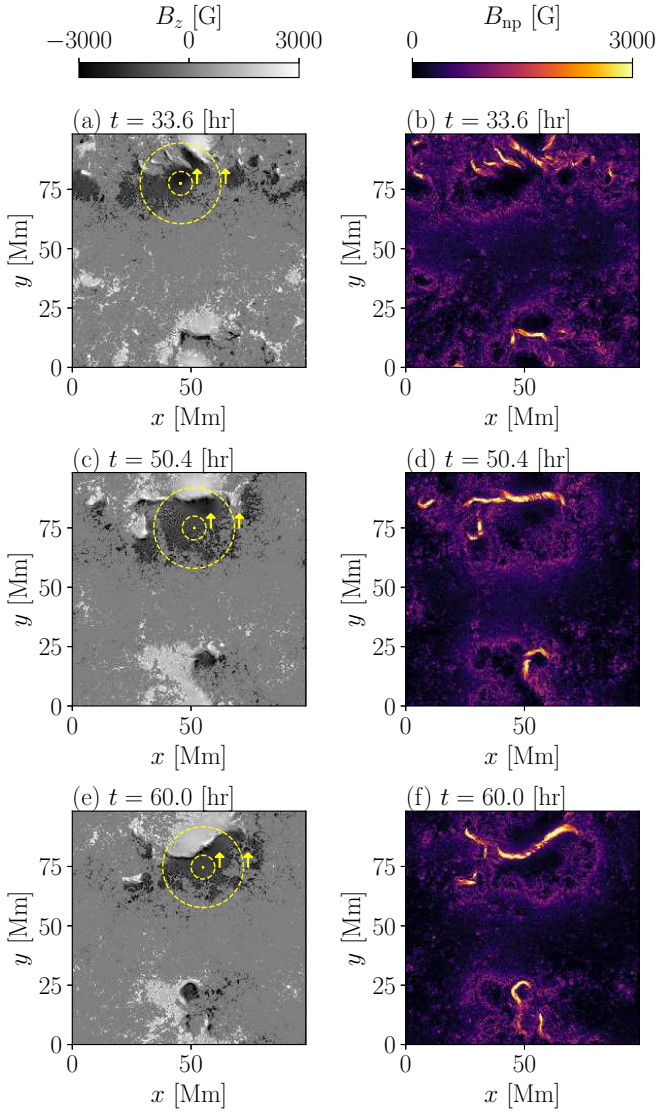


Figure 4. Panels (a)–(f) shows temporal evolution of B_z and B_{np} at the $\tau = 1$ surface in case 001. The yellow dashed circles are the slits used for Fig. 5.

(b), (d), and (f) show the spatial distribution and temporal evolution of B_{np} at the $\tau = 1$ surface. Strong nonpotential fields were localized around the polarity inversion lines. This feature was common to all the cases of parameter survey in this study, and to the actual active regions (Kusano et al. 2020).

3.2 Parameter Survey

We carried out 93 simulations with different initial flux tube positions. Figure 7 displays the distribution of the magnetic flux at the $\tau = 1$ surface for all 93 cases. Each panel shows the snapshot when the amount of flux was maximum in each case. We showed that various magnetic distributions are created only by the difference in the convective flows surrounding the flux tubes. We can find clear differences even between the cases in which the horizontal positions of the initial flux tubes were the same but the depths were different. In many cases, opposite-polarity fluxes collided in the photosphere, forming δ -type magnetic distribution. Some cases reproduced β -type magnetic distribution. Several cases resulted in no successful emer-

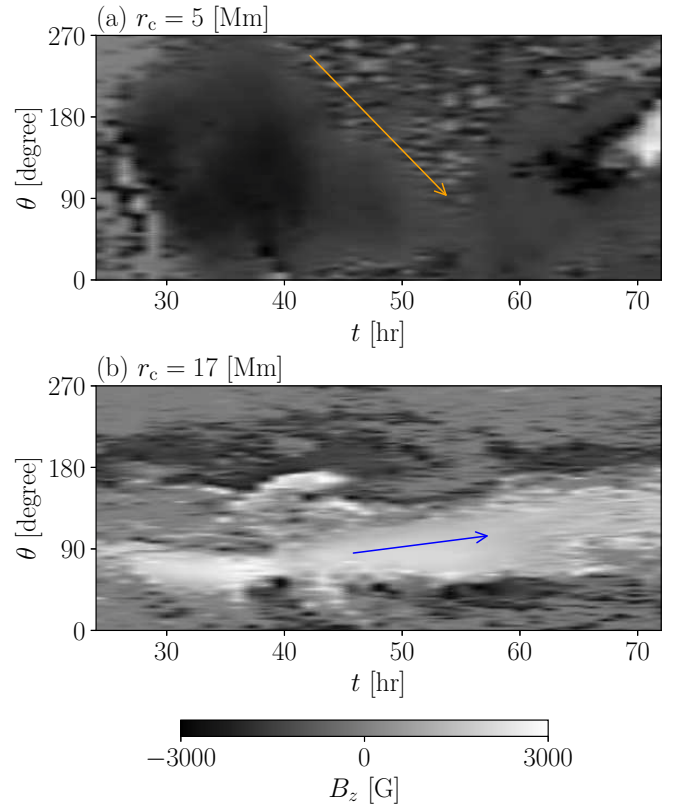


Figure 5. Time slice of the B_z map along the circular slits denoted by yellow dashed circles in Fig. 4 (a), (c) and (e). Panel (a) and (b) show the results with the slit radii $r_c = 5$ Mm and $r_c = 17$ Mm, respectively.

gence to the photosphere. In cases where the most of the initial flux tube was occupied by a downflow, the flux tube sank to the deep layer and never emerged to the photosphere.

Figure 8 (a) shows the temporal evolution of the unsigned magnetic flux at the $\tau = 1$ surface defined as follows:

$$\Phi = \int_{\tau=1} |B_z| dx dy. \quad (13)$$

Here we regarded the $\tau = 1$ surface as the horizontal plane because of the small height difference. In most cases, temporal profiles can be divided into emergence and decay phases, which are consistent with the previous observational and numerical studies (Iionidis et al. 2011; Otsuji et al. 2011; Centeno 2012; Toriumi et al. 2014b; Norton et al. 2017; Cheung et al. 2007, 2008; Rempel & Cheung 2014). We only focused on the emergence phase here because the decay phase was not covered in several cases during the calculation time. The black circles in Fig. 8 (b) represent $\max(\Phi)$ vs $\max(d\Phi/dt)$ in our simulations. The results revealed the scaling relationship of $d\Phi/dt \propto \Phi^{0.78}$. Figure 8 (b) also shows the results of the previous observational and numerical studies (the references are summarized in Norton et al. (2017)). The magnetic fluxes in our study covered relatively larger values than the results of the previous studies. The flux emergence rates in our results were several times larger than the observational values in the cases of the larger flux amount. Thus, the scaling exponent 0.78 in our results was larger than the observational value 0.57 reported by Otsuji et al. (2011).

We investigated the distribution trend of the magnetic nonpotential field in the photosphere. First, we derived the temporally averaged

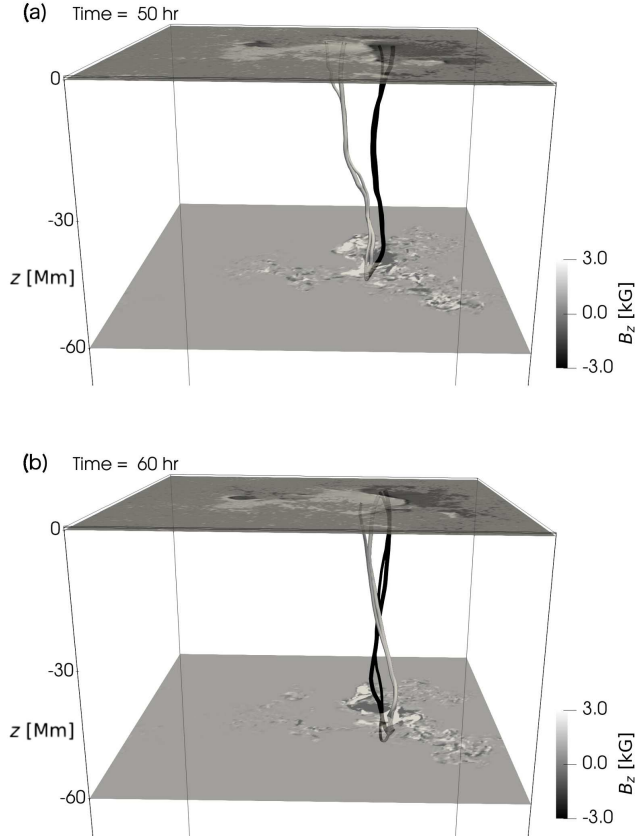


Figure 6. Evolution of magnetic field writhe in the convection zone.

nonpotential field in each case:

$$\langle B_{\text{np}} \rangle_t = \frac{1}{t_c} \int_0^{t_c} B_{\text{np}}(t, y, z) dt, \quad (14)$$

where t and t_c represent the time and duration of the simulation in each case, respectively. Note that t_c is different in each case. Figure 9 displays $\langle B_{\text{np}} \rangle_t$ in each case. To evaluate the trend of the B_{np} distribution, we summed $\langle B_{\text{np}} \rangle_t$ of all cases and normalized the sum:

$$\langle \langle B_{\text{np}} \rangle_t \rangle_{\text{case}} = F / F_{\text{max}}, \quad (15)$$

where

$$F = \sum_{\text{case}} \langle B_{\text{np}} \rangle_t, \quad (16)$$

and F_{max} is the maximum value of F . Figure 10 shows $\langle \langle B_{\text{np}} \rangle_t \rangle_{\text{case}}$. The regions where $\langle \langle B_{\text{np}} \rangle_t \rangle_{\text{case}}$ is close to unity have a higher possibility that a strong nonpotential field is created.

To investigate the cause of the $\langle \langle B_{\text{np}} \rangle_t \rangle_{\text{case}}$ distribution, we compared it with the mean velocity field in the convection zone. The mean velocity field $\langle \langle v_q \rangle_t \rangle_{\text{case}}$ was computed as follows:

$$\langle \langle v_q \rangle_t \rangle_{\text{case}} = \frac{1}{N} \sum_{\text{case}} \langle v_q \rangle_t, \quad (17)$$

$$\langle v_q \rangle_t = \frac{1}{t_c} \int_0^{t_c} v_q(t, x, y, z) dt, \quad (18)$$

where q denotes the component x , y , or z , and $N = 93$ is the number



Figure 7. B_z at the $\tau = 1$ surface of all cases at the time when the amount of magnetic flux was maximum in each case.

of the cases. Figure 11 shows $\langle \langle v_z \rangle_t \rangle_{\text{case}}$ at the different height. We also defined the horizontal divergence D_h and the vertical vorticity W_z of the mean field as follows:

$$D_h = \frac{\partial}{\partial x} \langle \langle v_x \rangle_t \rangle_{\text{case}} + \frac{\partial}{\partial y} \langle \langle v_y \rangle_t \rangle_{\text{case}}, \quad (19)$$

$$W_z = \frac{\partial}{\partial x} \langle \langle v_y \rangle_t \rangle_{\text{case}} - \frac{\partial}{\partial y} \langle \langle v_x \rangle_t \rangle_{\text{case}}. \quad (20)$$

Figures 12 and 13 show D_h and W_z at different heights. We calculated the correlation coefficients (CCs) of $\langle \langle B_{\text{np}} \rangle_t \rangle_{\text{case}}$ versus $\langle \langle v_z \rangle_t \rangle_{\text{case}}$, D_h , and W_z at each height, respectively. Figure 14 shows the CCs as a function of height. The sign of the CCs corresponds to the sign of $\langle \langle v_z \rangle_t \rangle_{\text{case}}$, D_h , and W_z because $\langle \langle B_{\text{np}} \rangle_t \rangle_{\text{case}}$ is always positive. $\langle \langle B_{\text{np}} \rangle_t \rangle_{\text{case}}$ had a negative correlation with $\langle \langle v_z \rangle_t \rangle_{\text{case}}$ over a broad range from $z = -100$ Mm to -20 Mm but peaked around $z =$

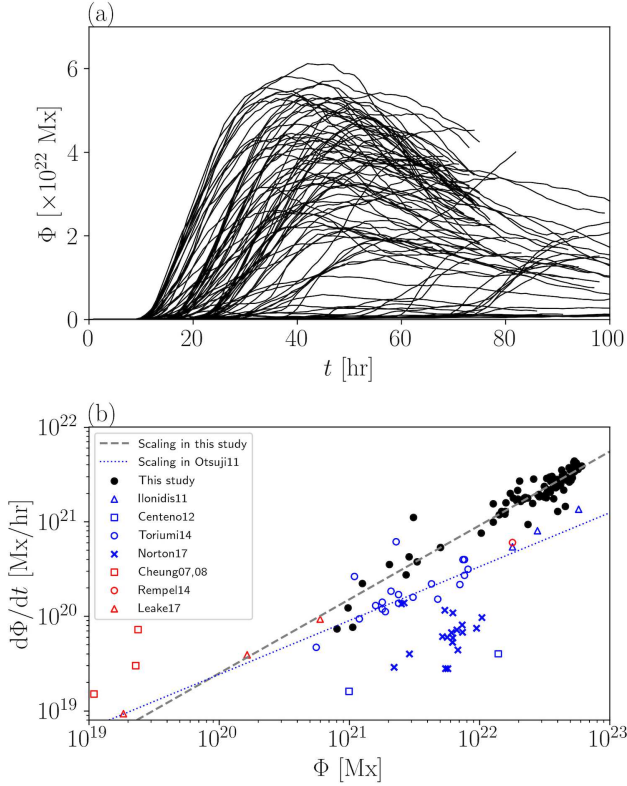


Figure 8. Panel (a) shows the temporal evolution of the unsigned magnetic flux Φ in each case. Panel (b) is the scatter plot of $\max(\Phi)$ versus $\max(d\Phi/dt)$. The plot shows the results of each case in this study (black circles), previous observations (red marks, Ilonidis et al. 2011; Centeno 2012; Toriumi et al. 2014b; Norton et al. 2017), and previous simulations (blue marks, Cheung et al. 2007, 2008; Rempel & Cheung 2014; Leake et al. 2017). The gray dashed line represents the scaling fitted to the results in this study. The blue dotted line represents the scaling in a previous observational study that analyzed over 100 samples (Otsuji et al. 2011).

–40 Mm (CC ~ -0.7). This indicates the relationship between the nonpotential field in the photosphere and the downflow rooted to the deep layer in the convection zone. $\langle\langle B_{np} \rangle\rangle_t$ had a weak or no correlation with D_h and W_z .

It is likely that small-scale fluctuations reduce CCs to smaller values. We excluded the small-scale structures from $\langle\langle v_z \rangle\rangle_t$ using a low-pass filter. The low-pass filter was applied in the two-dimensional horizontal plane at each height. Figure 15 shows the filtered $\langle\langle v_z \rangle\rangle_t$ including $f < f_{\text{cutoff}} = 1.44 \times 10^{-2} \text{ Mm}^{-1}$ where $f (= 1/\lambda)$ represents the wavenumber (λ represents the wavelength) and f_{cutoff} is the cutoff wavenumber. The distributions at $z = -2.0 \text{ Mm}$, -10 Mm , and -40 Mm (panels (a), (b), and (c)) are similar to each other. Figure 16 (a) shows the correlation between $\langle\langle B_{np} \rangle\rangle_t$ and the filtered $\langle\langle v_z \rangle\rangle_t$ as a function of height. It shows a strong correlation ($|CC| > 0.8$) in $x > -48 \text{ Mm}$. Figure 16 (b) shows the CC as a function of height and cutoff wavenumber of the low-pass filter. $|CC| > 0.8$ is found in the parameter space of $-48 \text{ Mm} < x < 0$ and $f_{\text{cutoff}} < 0.02 \text{ Mm}^{-1}$ (inside the dashed line in Fig. 16 (b)) corresponding to the region and the spatial scale of the downflow plume $\sim 50 \text{ Mm}$.

Figure 17 shows the filtered D_h including $f < f_{\text{cutoff}} = 1.44 \times 10^{-2} \text{ Mm}^{-1}$. The filtered D_h shared the similar distribution at $z = -2.0 \text{ Mm}$, -10 Mm , and -40 Mm (Fig. 17 (a), (b), and (c)).



Figure 9. Temporally averaged nonpotential field $\langle B_{np} \rangle_t$ at the $\tau = 1$ surface of all cases.

They were also similar to the filtered $\langle\langle v_z \rangle\rangle_t$ at $z = -2.0 \text{ Mm}$, -10 Mm , and -40 Mm (Fig. 15 (a), (b), and (c)). Figure 18 shows the correlation between $\langle\langle B_{np} \rangle\rangle_t$ and the filtered D_h . $CC < -0.8$, which indicates a strong correlation between the nonpotential field and horizontal converging flows, was found at $z > -30 \text{ Mm}$ and $f_{\text{cutoff}} < 0.02 \text{ Mm}^{-1}$.

In the deep convection zone, the anelastic approximation $\nabla \cdot (\rho_0 \mathbf{v}) = 0$ is valid. The relationship between the downflow plume and the horizontal converging flows is formulated as follows (Lord et al. 2014):

$$\begin{aligned}
 0 &= \nabla \cdot (\rho_0 \mathbf{v}), \\
 &= \nabla_h \cdot (\rho_0 \mathbf{v}_h) + \partial_z (\rho_0 v_z), \\
 &= \rho_0 \nabla_h \cdot \mathbf{v}_h + v_z \partial_z \rho_0 + \rho_0 \partial_z v_z, \\
 \Leftrightarrow \nabla_h \cdot \mathbf{v}_h &= \frac{v_z}{H_\rho} - \partial_z v_z.
 \end{aligned} \tag{21}$$

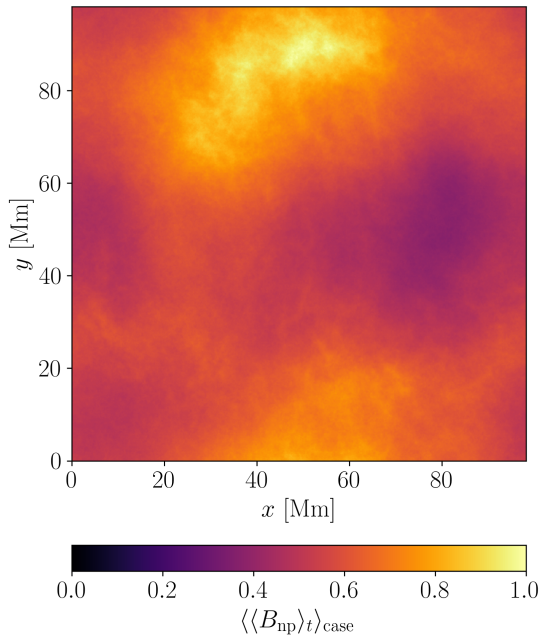


Figure 10. Distribution of $\langle\langle B_{np} \rangle\rangle_t$ (see Eqs. (14)–(16)).

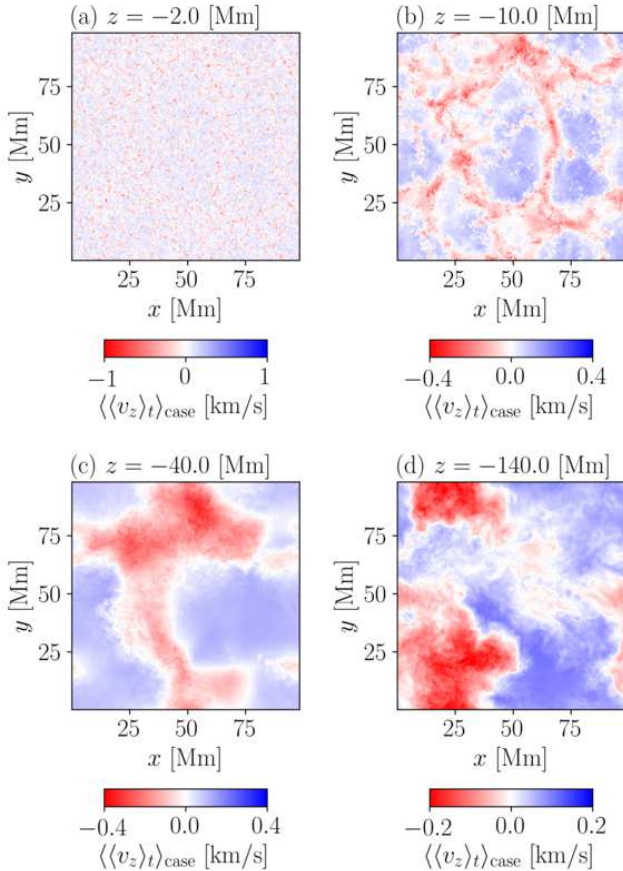


Figure 11. Mean vertical velocity $\langle\langle v_z \rangle\rangle_t$ at different heights (see Eqs. (17)–(18)).

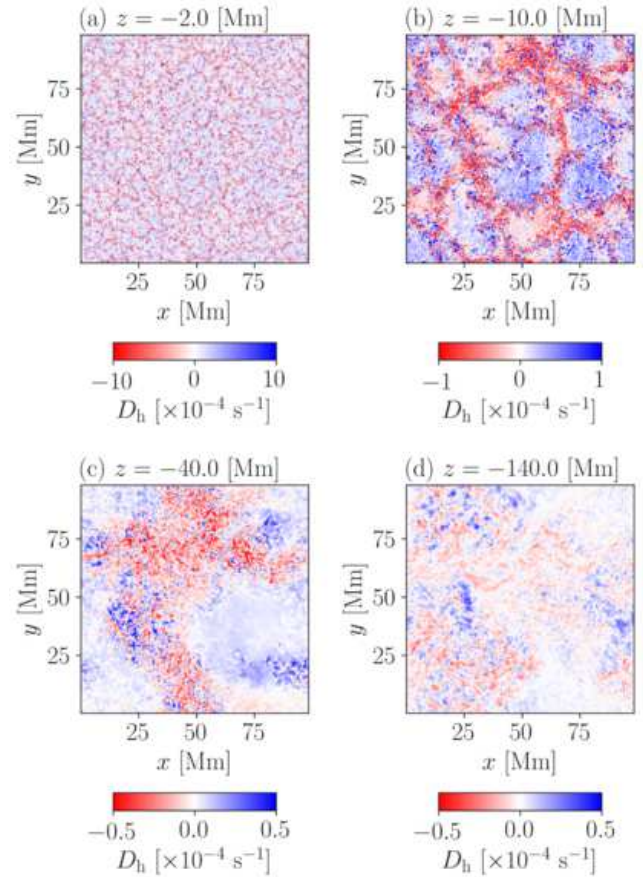


Figure 12. Horizontal divergence of mean velocity field D_h at different heights (see Eq. (19)).

where \mathbf{v}_h represents the horizontal velocity and $H_\rho = -(\partial \ln \rho_0 / \partial z)^{-1}$ is the scale height. We assume $v_z / H_\rho \gg \partial_z v_z$ for the downflow whose spatial scale is much larger than the scale height. Thus, we obtain the following equation:

$$\nabla_h \cdot \mathbf{v}_h = \frac{v_z}{H_\rho}. \quad (22)$$

Equation (22) indicates that large-scale downflow (negative v_z) is followed by the horizontal converging flows. D_h and $\langle\langle B_{np} \rangle\rangle_t$ are strongly correlated when v_z is strongly correlated with $\langle\langle B_{np} \rangle\rangle_t$.

Figure 19 shows the filtered W_z including $f < f_{\text{cutoff}} = 1.44 \times 10^{-2} \text{ Mm}^{-1}$. The distributions at $z = -2 \text{ Mm}$ and $z = -10 \text{ Mm}$ are similar, but the distributions at $z = -40 \text{ Mm}$ and $z = -140 \text{ Mm}$ are different from the two shallow distributions. The distributions are also different from the filtered $\langle\langle v_z \rangle\rangle_t$ and D_h distributions in Figs. 15 and 17. Figure 20 shows the correlation between $\langle\langle B_{np} \rangle\rangle_t$ and filtered W_z . The correlation coefficients do not exceed 0.8 at any height or f_{cutoff} . This result suggests that the vertical vortices of the convective flows were not the origin of the $\langle\langle B_{np} \rangle\rangle_t$ distribution.

We also compared $\langle\langle B_{np} \rangle\rangle_t$ with the convective velocity field at the initial state $t = 0$. The convective velocity field at $t = 0$, common for all cases, was not affected by the magnetic field. Figure 21 shows the CCs of the filtered distributions of v_z and $\nabla_h \cdot \mathbf{v}_h$ ($f_{\text{cutoff}} = 1.44 \times 10^{-2} \text{ Mm}^{-1}$) against $\langle\langle B_{np} \rangle\rangle_t$. CCs in $x > -50 \text{ Mm}$ are approximately -0.7 . This result suggests that the place creating the photospheric nonpotential fields depends on the distribution of the downflow plume extending to the convection zone within the depth of -50 Mm . The results also suggest that the photospheric nonpotential

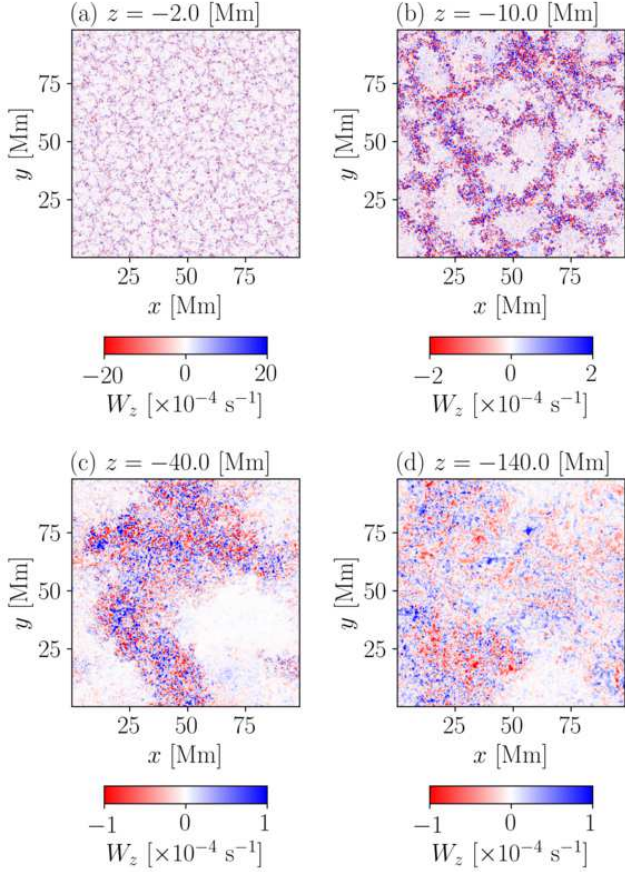


Figure 13. Vertical vorticity of mean velocity field W_z at different heights (see Eq. (20)).

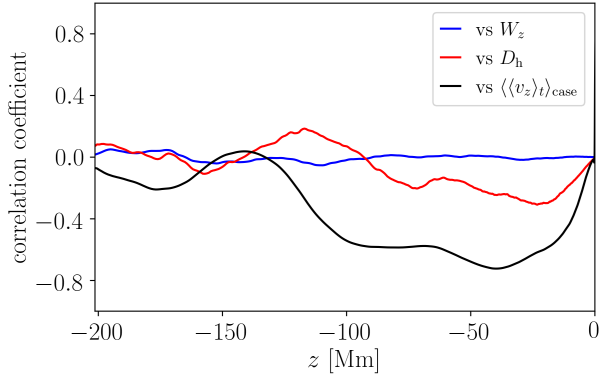


Figure 14. Correlation coefficients of $\langle v_z \rangle_t$ _{case} vs $\langle B_{np} \rangle_t$ _{case} (black line), D_h vs $\langle B_{np} \rangle_t$ _{case} (red line), W_z vs $\langle B_{np} \rangle_t$ _{case} (blue line) as a function of height.

field distribution can be predicted by detecting the downflow plume or horizontal converging flows even before the flux appears in the photosphere.

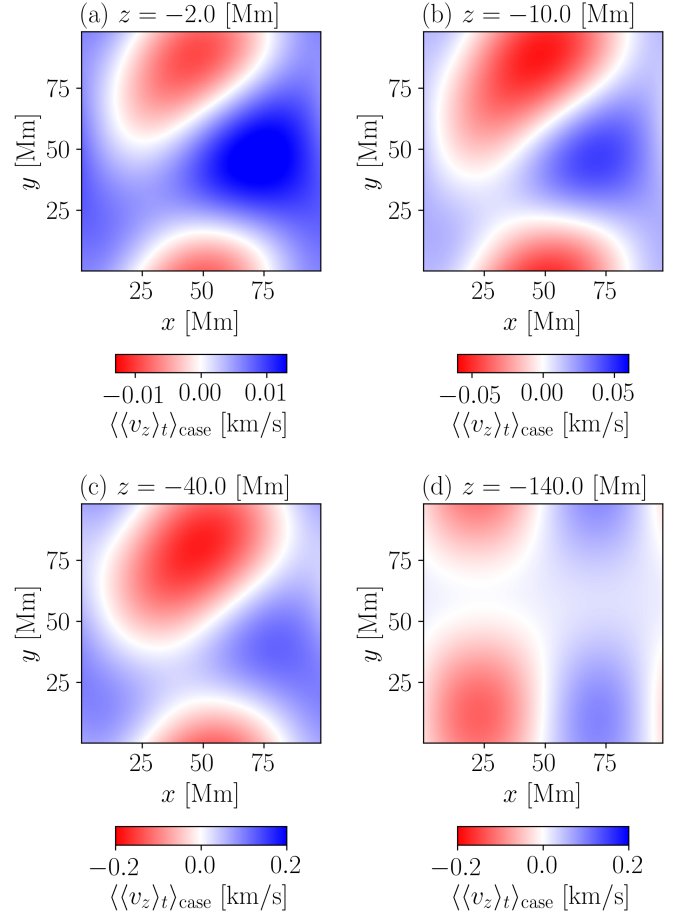


Figure 15. $\langle v_z \rangle_t$ _{case} excluding small-scale structures using a low-pass filter with $f_{\text{cutoff}} = 1.44 \times 10^{-2} \text{ Mm}^{-1}$. The panels show the filtered $\langle v_z \rangle_t$ _{case} at different heights.

4 SUMMARY AND DISCUSSION

We carried out 93 radiative MHD simulations reproducing the transport of the magnetic flux tubes in the solar convection zone to the photosphere. Various types of magnetic distributions including δ -type and β -type were reproduced in the photosphere only by the difference in the convective flows surrounding the flux tubes. In this study, we adopted the convective velocity field including a persistent large-scale downflow plume as the initial state. In the cases where the flux tubes were trapped by the downflow plume, the δ -type magnetic distribution with the strong nonpotential field was created in the photosphere due to the collision of positive and negative fluxes. The previous studies (Fan 2009; Sturrock et al. 2015; Toriumi & Hotta 2019) found the unipolar rotation of the sunspots transporting the magnetic helicity from the convection zone to the corona. We newly found the bipolar rotation of the δ -spots whose direction is opposite to the unipolar rotation. The bipolar rotation was driven by the conversion of twist to writhe. In our parameter survey, the δ -type magnetic distribution was more frequently observed than the β -type distribution. There were also cases without flux emergence when the initial position of the flux tubes was just below the downflow plumes, and most of the flux tube body was filled with downflow.

Using the results of the statistical analysis, we derived the distribution of the nonpotential field $\langle B_{np} \rangle_t$ _{case} in the photosphere. The comparison with the mean velocity field in the convection zone

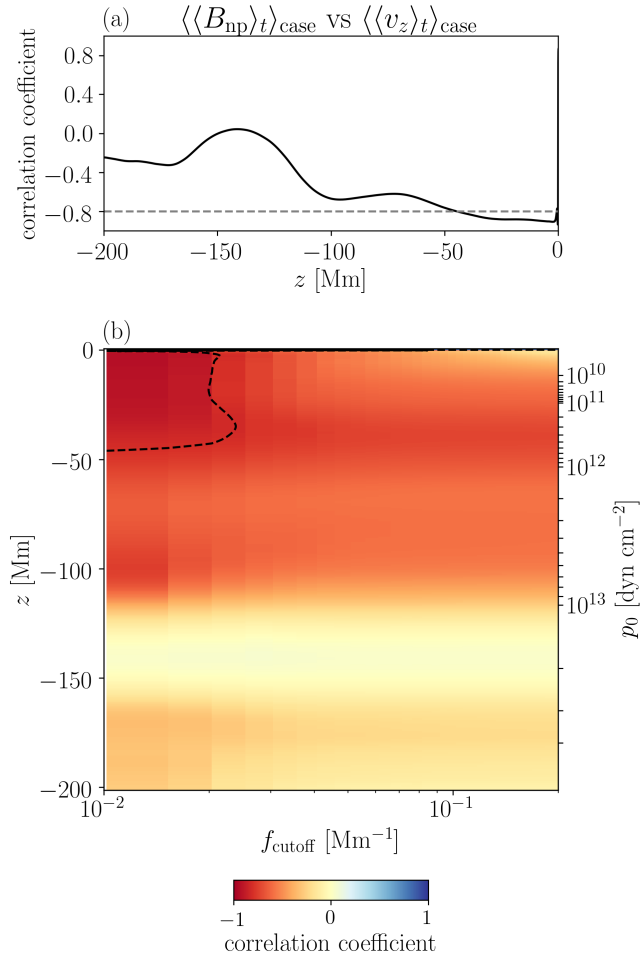


Figure 16. Correlation between filtered $\langle\langle v_z \rangle_t\rangle_{\text{case}}$ and $\langle\langle B_{\text{np}} \rangle_t\rangle_{\text{case}}$. Panel (a) shows the correlation coefficients as a function of height with $f_{\text{cutoff}} = 1.44 \times 10^{-2} \text{ Mm}^{-1}$. Panel (b) shows the correlation coefficients as a function of height and f_{cutoff} . The dashed lines in panels (a) and (b) denote $\text{CC} = -0.8$.

revealed that $\langle\langle B_{\text{np}} \rangle_t\rangle_{\text{case}}$ was strongly correlated with the distribution of the downflow plumes in the convection zone. The distribution of the horizontal converging flows also showed a strong correlation with $\langle\langle B_{\text{np}} \rangle_t\rangle_{\text{case}}$. The results support the scenario that the non-potential field is formed by the collision of opposite-polarity magnetic fluxes trapped by the downflow plume (Toriumi & Hotta 2019; Hotta & Toriumi 2020). The horizontal converging flow gathers the emerging flux tubes into the downflow region. Hence, the destination of the emerging flux tube was most likely above the downflow plumes.

In the analyses, we regarded the $\tau = 1$ surface as a flat surface. We evaluated the impact of this assumption on our results. In case 001, for example, the average $\tau = 1$ surface was 67 km at $t = 50$ h. The grid point closest to the average $\tau = 1$ surface was at $z = 52$ km. The difference of the magnetic flux was $|\Phi^\tau - \Phi^z|/\Phi^z = 0.06$, where the superscripts τ and z represent the values at the average $\tau = 1$ surface and at $z = 52$ km, respectively. The mean squared errors of B_x^τ vs B_x^z , B_y^τ vs B_y^z , and B_z^τ vs B_z^z , were 50.0 G, 63.3 G, and 50.2 G, respectively. The mean squared error of B_{np}^τ vs B_{np}^z was 99.4 G. The correlation coefficients of B_x^z vs B_x^τ , B_y^z vs B_y^τ , and B_z^z vs B_z^τ were 0.98, 0.91, and 0.95, respectively. The correlation

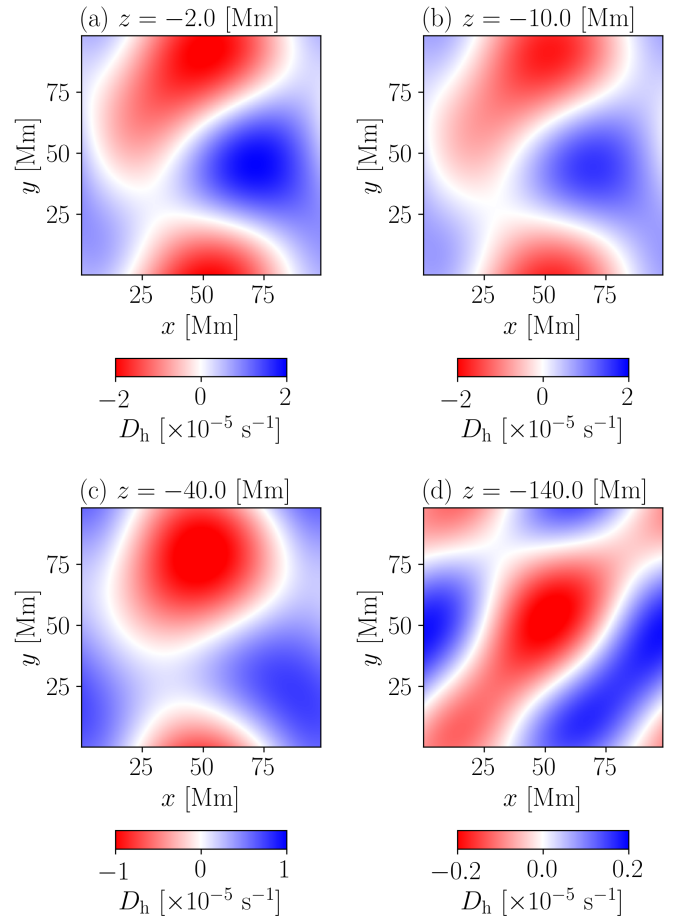


Figure 17. Same as Fig. 15 but for D_h .

coefficient of $\langle B_{\text{np}} \rangle_t^z$ vs $\langle B_{\text{np}} \rangle_t^\tau$ was 0.9. In the other cases as well as case 001, the difference of the magnetic flux was a few percent, and the correlation coefficient between $\langle B_{\text{np}} \rangle_t^z$ vs $\langle B_{\text{np}} \rangle_t^\tau$ was over 0.9. Therefore, we conclude that the magnetic fluxes and the correlation between $\langle\langle B_{\text{np}} \rangle_t\rangle_{\text{case}}$ and $\langle\langle v_z \rangle_t\rangle_{\text{case}}$ are not significantly changed if we compute those values using the magnetic field data at a certain height close to the solar surface.

The correlation between $\langle\langle B_{\text{np}} \rangle_t\rangle_{\text{case}}$ and the distribution of the downflow plume before flux emergence ($|\text{CC}| \sim 0.7$) suggests that high free energy regions in the photosphere can be predicted before flux emergence by detecting the downflow plume in the convection zone. In our simulation, $t = 0$ was 20–30 h before flux emergence; i.e., the leading time was almost one day. The leading time depends on the persistence of the downflow plume. Previous studies that used helioseismic techniques detected the signals of the emerging fluxes in the subsurface layer before the flux appeared in the photosphere (Ilonidis et al. 2011; Birch et al. 2013; Toriumi et al. 2013). The signals were not detected in the quiet Sun without flux emergence. Ilonidis et al. (2011) reported that the signals of the emerging fluxes were mainly contributed by the acoustic waves at the depth of 57–60 Mm, and they were concentrated in the area with a size of 30–50 Mm in the horizontal direction. Our simulation results were quantitatively consistent with the observational results of previous studies.

The detection of the pre-emerging regions is still challenging. We have to select local candidate areas to apply the helioseismic analysis in the solar hemisphere; however, there are few clues to

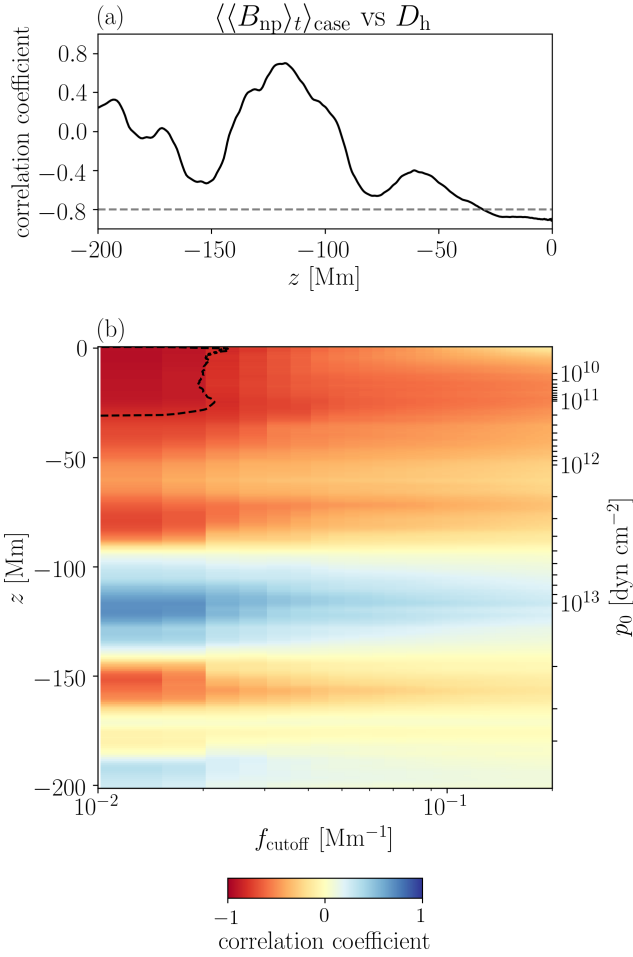


Figure 18. Same as Fig. 16 but for D_h .

determine them before the flux emergence. Our findings are helpful to limit the regions where helioseismic analysis should be applied and contribute to increase the efficiency for successful detection of pre-emerging regions in the solar hemisphere. Helioseismology can be used to detect the horizontal flows rather than the vertical flows. Hence, the correlation between the horizontal converging flows and $\langle\langle B_{np}\rangle\rangle_t$ can improve the practical detection. Even if we cannot detect the flux emergence beforehand, we can still predict that the emerging flux most likely develops into a δ -spot.

In actual observations, β -spots are more frequently detected, whereas in our parameter survey, δ -spots were more frequently observed. Two factors determine where the δ -spots favorably form. One is the downflow plume in the convection zone; the other factor is the birthplace of the flux tubes. In this study, the initial positions of the flux tubes were assumed to be uniformly distributed, and thus, there is the possibility that the flux tubes are located in the regions where they do not actually exist. Our results imply that there should be favorable locations of the birthplace of the flux tubes. The theoretical findings and previous numerical simulations suggested that the toroidal magnetic field of the flux tubes can be created at the overshoot region in the tachocline (Fan 2021). The exact region where the flux tubes are generated is still under debate. Further investigation using dynamo simulation is required to constrain the birthplace of the flux tubes. The periodic boundary in our simulations can also

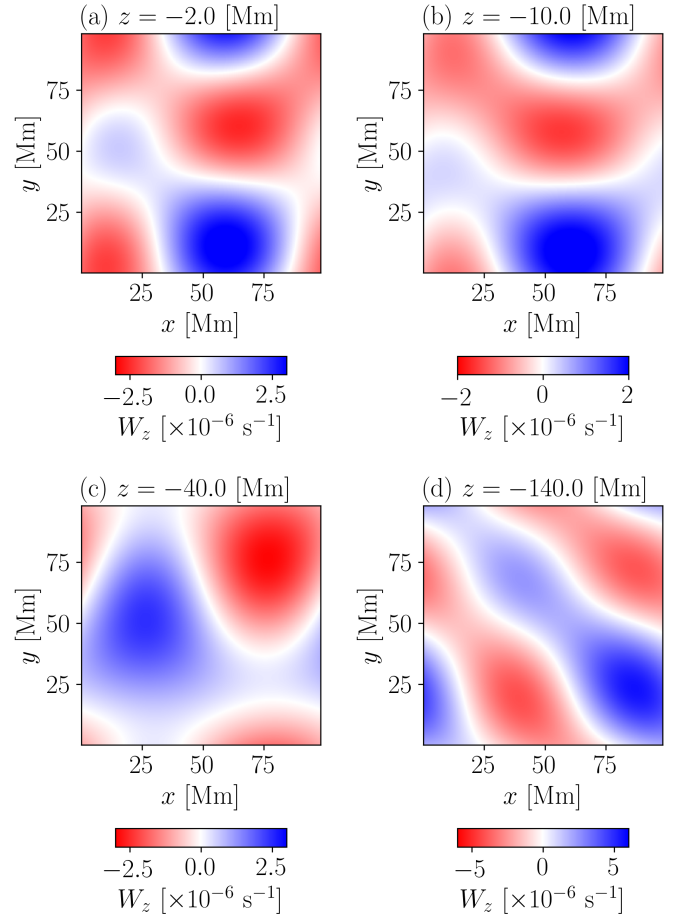


Figure 19. Same as Fig. 15 but for W_z .

be the reason why the δ -spots were more frequently created. Due to the periodic boundary, magnetic fluxes that left from one side of the simulation domain reentered from the opposite side, leading to the higher frequency of the flux collision. This process occurred in Toriumi & Hotta (2019), but it was not always the case in this study.

As shown in Fig. 8, our results covered relatively larger amount of magnetic fluxes. The flux emergence rates in our results were several times larger than the observational values, resulting in larger scaling exponents than the previous observational results of Otsuji et al. (2011). Most of the simulated results including those of the previous studies showed larger emergence rates because the simulated turbulent velocity was faster than the realistic value, and the initial flux tube model was simple. We assumed the straight flux tube with uniform field strength along the axis in the initial state, but the actual flux tube created in the convection zone should have the nonuniform field strength and the curved geometry. To include the realistic flux tube model, the numerical setting adopted in Chen et al. (2017), where the initial flux tube model referred a result of a dynamo simulation, should be used. The other possibility is that the observational values had too large dispersion to obtain the robust scaling exponent. Our simulated results, where the initial turbulent velocity fields were common, showed relatively smaller dispersion. The observational values in Fig. 8 include the results from different active regions in different places and times; thus, turbulence conditions can be different in each case. The method of data analysis can also affect the results, e.g., Otsuji et al. (2011) used the data of the maximum Φ versus the temporally averaged $d\Phi/dt$ for the fitting, while we used

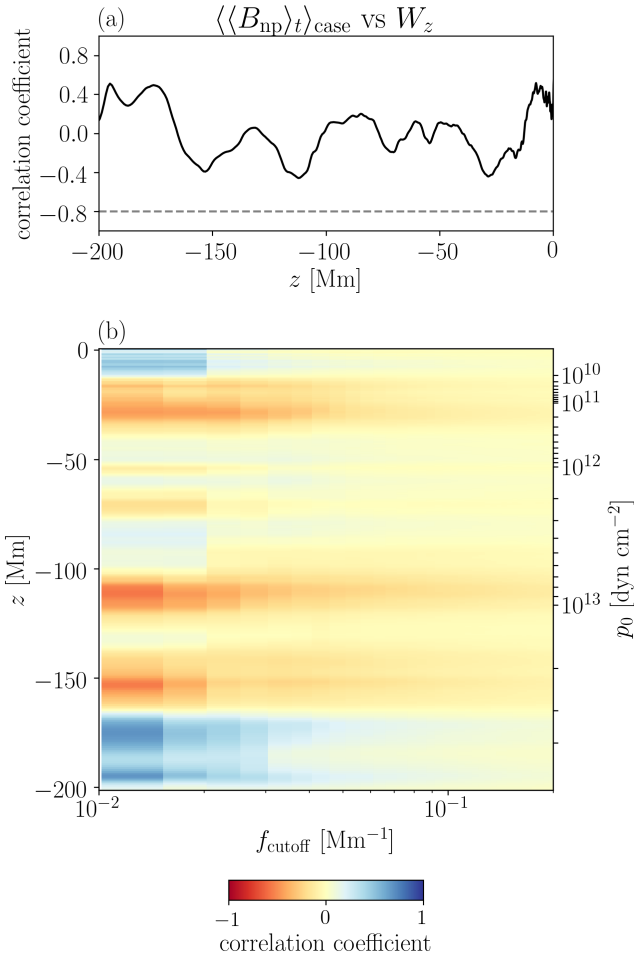


Figure 20. Same as Fig. 16 but for W_z

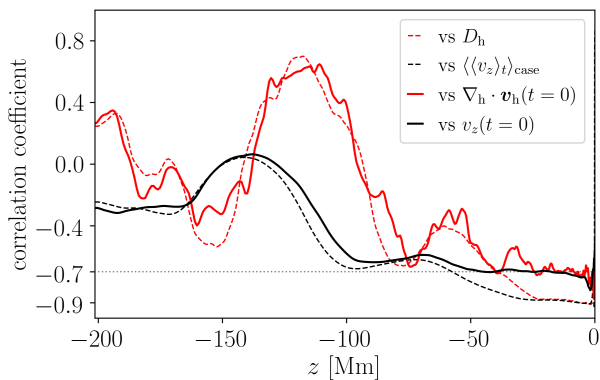


Figure 21. Correlation coefficients as a function of height. Black solid line: $v_z(t=0)$ vs $\langle\langle B_{np}\rangle\rangle_t$ case, red solid line: lowpass-filtered $\nabla_h \cdot \mathbf{v}_h(t=0)$ vs $\langle\langle B_{np}\rangle\rangle_t$ case, black dashed line: $\langle\langle v_z\rangle\rangle_t$ case vs $\langle\langle B_{np}\rangle\rangle_t$ case (same as Fig. 16 (a)), red dashed line: D_h vs $\langle\langle B_{np}\rangle\rangle_t$ case (same as Fig. 18 (a)).

the data of the maximum Φ versus the maximum $d\Phi/dt$. Further statistical studies are required to unravel the impacts of turbulence and magnetic geometry on the relationship between Φ and $d\Phi/dt$ from both observational and numerical perspectives.

ACKNOWLEDGEMENTS

We thank the referee for the constructive comments. This work was supported by MEXT as “Program for Promoting Researches on the Supercomputer Fugaku” (Toward a unified view of the universe: from large scale structure to planets, Elucidation of solar and planetary dynamics and evolution, grant no. 20351188), JSPS KAKENHI Grant Nos. JP20KK0072 (PI: S. Toriumi), JP21H01124 (PI: T. Yokoyama), JP20K14510 (PI: H. Hotta), JP21H04497 (PI: H. Miyahara) and JP21H04492 (PI: K. Kusano), and the NINS program for cross-disciplinary study (Grant Nos. 01321802 and 01311904) on Turbulence, Transport, and Heating Dynamics in Laboratory and Astrophysical Plasmas: “SoLaBo-X. TK was supported by the National Center for Atmospheric Research, which is a major facility sponsored by the National Science Foundation under Cooperative Agreement No. 1852977. A part of this study was carried out using the computational resources of the Center for Integrated Data Science, Institute for Space-Earth Environmental Research, Nagoya University. We would like to thank Editage (www.editage.com) for English language editing.

DATA AVAILABILITY

Data available on request.

REFERENCES

- Amari T., Luciani J. F., Mikic Z., Linker J., 2000, *ApJ*, **529**, L49
 Amari T., Canou A., Aly J.-J., 2014, *Nature*, **514**, 465
 Berger M. A., Prior C., 2006, *Journal of Physics A Mathematical General*, **39**, 8321
 Birch A. C., Braun D. C., Leka K. D., Barnes G., Javornik B., 2013, *ApJ*, **762**, 131
 Centeno R., 2012, *ApJ*, **759**, 72
 Chen F., Rempel M., Fan Y., 2017, *ApJ*, **846**, 149
 Cheung M. C. M., Schüssler M., Moreno-Insertis F., 2007, *A&A*, **467**, 703
 Cheung M. C. M., Schüssler M., Tarbell T. D., Title A. M., 2008, *ApJ*, **687**, 1373
 Cheung M. C. M., Rempel M., Title A. M., Schüssler M., 2010, *ApJ*, **720**, 233
 Christensen-Dalsgaard J., et al., 1996, *Science*, **272**, 1286
 DeVore C. R., Antiochos S. K., 2000, *ApJ*, **539**, 954
 Fan Y., 2001, *ApJ*, **554**, L111
 Fan Y., 2009, *ApJ*, **697**, 1529
 Fan Y., 2021, *Living Reviews in Solar Physics*, **18**, 5
 Fan Y., Gibson S. E., 2007, *ApJ*, **668**, 1232
 Fang F., Fan Y., 2015, *ApJ*, **806**, 79
 Georgoulis M. K., Titov V. S., Mikić Z., 2012, *ApJ*, **761**, 61
 Hotta H., Iijima H., 2020, *MNRAS*, **494**, 2523
 Hotta H., Toriumi S., 2020, *MNRAS*, **498**, 2925
 Hotta H., Rempel M., Yokoyama T., Iida Y., Fan Y., 2012, *A&A*, **539**, A30
 Hotta H., Rempel M., Yokoyama T., 2015, *ApJ*, **798**, 51
 Hotta H., Iijima H., Kusano K., 2019, *Science Advances*, **5**, 2307
 Iijima H., Hotta H., Imada S., 2019, *A&A*, **622**, A157
 Ilonidis S., Zhao J., Kosovichev A., 2011, *Science*, **333**, 993
 Jiang C., Wu S. T., Feng X., Hu Q., 2016, *Nature Communications*, **7**, 11522
 Kaneko T., Yokoyama T., 2014, *ApJ*, **796**, 44
 Kaneko T., Park S.-H., Kusano K., 2021, *ApJ*, **909**, 155

- Kusano K., Bamba Y., Yamamoto T. T., Iida Y., Toriumi S., Asai A., 2012, [ApJ](#), **760**, 31
- Kusano K., Iju T., Bamba Y., Inoue S., 2020, [Science](#), **369**, 587
- Leake J. E., Linton M. G., Schuck P. W., 2017, [ApJ](#), **838**, 113
- Leka K. D., Canfield R. C., McClymont A. N., van Driel-Gesztelyi L., 1996, [ApJ](#), **462**, 547
- Lord J. W., Cameron R. H., Rast M. P., Rempel M., Roudier T., 2014, [ApJ](#), **793**, 24
- Magara T., Longcope D. W., 2003, [ApJ](#), **586**, 630
- Manek B., Brummell N., 2021, [ApJ](#), **909**, 72
- Norton A. A., Jones E. H., Linton M. G., Leake J. E., 2017, [ApJ](#), **842**, 3
- Otsuji K., Kitai R., Ichimoto K., Shibata K., 2011, [PASJ](#), **63**, 1047
- Park S.-H., Guerra J. A., Gallagher P. T., Georgoulis M. K., Bloomfield D. S., 2018, [Sol. Phys.](#), **293**, 114
- Rempel M., 2014, [ApJ](#), **789**, 132
- Rempel M., Cheung M. C. M., 2014, [ApJ](#), **785**, 90
- Rempel M., Schüssler M., Knölker M., 2009, [ApJ](#), **691**, 640
- Rogers F. J., Swenson F. J., Iglesias C. A., 1996, [ApJ](#), **456**, 902
- Sammis I., Tang F., Zirin H., 2000, [ApJ](#), **540**, 583
- Schmieder B., et al., 1994, [Sol. Phys.](#), **150**, 199
- Stein R. F., Nordlund A., 1989, [ApJ](#), **342**, L95
- Sturrock Z., Hood A. W., Archontis V., McNeill C. M., 2015, [A&A](#), **582**, A76
- Takasao S., Fan Y., Cheung M. C. M., Shibata K., 2015, [ApJ](#), **813**, 112
- Toriumi S., Hotta H., 2019, [ApJ](#), **886**, L21
- Toriumi S., Takasao S., 2017, [ApJ](#), **850**, 39
- Toriumi S., Wang H., 2019, [Living Reviews in Solar Physics](#), **16**, 3
- Toriumi S., Ilonidis S., Sekii T., Yokoyama T., 2013, [ApJ](#), **770**, L11
- Toriumi S., Iida Y., Kusano K., Bamba Y., Imada S., 2014a, [Sol. Phys.](#), **289**, 3351
- Toriumi S., Hayashi K., Yokoyama T., 2014b, [ApJ](#), **794**, 19
- Toriumi S., Schrijver C. J., Harra L. K., Hudson H., Nagashima K., 2017, [ApJ](#), **834**, 56
- Vögler A., Shelyag S., Schüssler M., Cattaneo F., Emonet T., Linde T., 2005, [A&A](#), **429**, 335
- Wheatland M. S., 2000, [ApJ](#), **532**, 616
- Zirin H., Liggett M. A., 1987, [Sol. Phys.](#), **113**, 267

This paper has been typeset from a $\text{\TeX}/\text{\LaTeX}$ file prepared by the author.